

# Cluster-based network model of an incompressible mixing layer

**Hao Li<sup>1,2</sup>, Daniel Fernex<sup>3</sup>, Jianguo Tan<sup>1</sup>,  
Marek Morzyński<sup>4</sup> and Bernd R. Noack<sup>5,2,3†</sup>**

<sup>1</sup> Science and Technology on Scramjet Laboratory,  
National University of Defense Technology, Changsha, Hunan Province, China

<sup>2</sup> Hermann-Fttinger-Institut, Technische Universität Berlin,  
Müller-Breslau-Straße 8, D-10623 Berlin, Germany

<sup>3</sup> Institut für Strömungsmechanik, Technische Universität Braunschweig,  
Hermann-Blenk-Straße 37, D-38108 Braunschweig, Germany

<sup>4</sup> Chair of Virtual Engineering, Poznań University of Technology,  
Jana Pawła II 24 street, 60-965 Poznań, Poland

<sup>5</sup> LIMSI, CNRS, Université Paris-Saclay, Bât 507,  
rue du Belvédère, Campus Universitaire, F-91403 Orsay, France

(Received ?; revised ?; accepted ?. - To be entered by editorial office)

We propose an automatable data-driven methodology for robust nonlinear reduced-order modeling from time-resolved snapshot data. In the kinematical coarse-graining, the snapshots are clustered into few centroids representable for the whole ensemble. The dynamics is conceptualized as a directed network where the centroids represent nodes and the directed edges denote possible finite-time transitions. The transition probabilities and times are inferred from the snapshot data. The resulting cluster-based network model constitutes a deterministic-stochastic grey-box model resolving the coherent-structure evolution. This model is motivated by limit-cycle dynamics, illustrated for the chaotic Lorenz attractor and successfully demonstrated for the laminar two-dimensional mixing layer featuring Kelvin-Helmholtz vortices and vortex pairing. Cluster-based network modeling opens a promising new avenue with unique advantages over other model-order reductions based on clustering or proper orthogonal decomposition.

## 1. Introduction

We propose a cluster-based network model (CNM) from time-resolved snapshot data exemplified for a laminar mixing layer. The goal is purely data-driven reduced-order modeling trading the physical insights from first principles, e.g., the Galerkin method (see, e.g. Holmes *et al.* 2012), with simplicity, robustness and closeness to the original data.

The mixing layer is an archetypical flow configuration associated with many academic and industrial applications. The flow is discussed virtually in any textbook of fluid mechanics. In the early stage, the laminar mixing layer gives rise to periodic, spatially growing Kelvin-Helmholtz vortices as described in stability theory (Michalke 1964), by vortex models (Hama 1962) or by a Proper Orthogonal Decomposition (POD) Galerkin model (Noack *et al.* 2005). At later stages, multiple vortex pairings induce the inverse cascade to lower wavenumbers and frequencies (Coats 1997). In addition, three-dimensional instabilities enrich the coherent structures by rib vortices and spanwise waviness (see,

† Email address for correspondence: jianguotan@nudt.edu.cn, bernd.noack@limsi.fr

e.g., Liu 1989). These mixing layer structures may be seen in the near-field region of wakes and jets. Moreover, control of most shear flows, including bluff-body wakes and jets, is based on an effective manipulation of the mixing layer (Fiedler 1990).

Since many decades, the mixing layer has been a challenging benchmark for reduced-order modeling, e.g. parabolized stability equations (Sasaki *et al.* 2018), vortex filament models (Ashurst & Meiburg 1988), POD models (Delville *et al.* 1999; Ukeiley *et al.* 2001; Wei & Rowley 2009), and cluster-based reduced-order models (Kaiser *et al.* 2014). Already the laminar two-dimensional shear layer can give rise to multiple frequencies (Kasten *et al.* 2016). The early stages of the convectively unstable dynamics are well resolved by parabolized stability and vortex filament models, requiring little empirical input. Turbulent dynamics may be resolved by data-driven approaches, e.g. POD or cluster-based models. POD Galerkin methods are intimately tied with the Navier-Stokes equations. While the kinematics, the modal expansion, is distilled from data, the temporal dynamics may be derived from first principles. Yet, the modal expansion encapsulates a convection dominated dynamics in an elliptic approach. This mismatch between modeling approach and dynamics is the root cause of the fragility of data-driven Galerkin models (Noack 2016). For the mixing layer, the lack of robustness is particularly pronounced as exhibited by modelled transients which are orders of magnitudes too large (Noack *et al.* 2005). Moreover, the time integration of the Galerkin model may easily lead to states far away from the training data, i.e., outside the region of model validity.

This robustness challenge of elliptical approaches is avoided by cluster-based reduced-order models (CROM) pioneered by Burkardt *et al.* (2006). Here, the state is coarse-grained to a small number of centroids representative for the whole ensemble of snapshots. Hence, modelled states will be close to the training data by the very construction. The potential of an extrapolation, e.g. predicting larger fluctuation amplitudes, is traded for robustness, i.e., staying close to the snapshot data.

In a CROM for the mixing layer (Kaiser *et al.* 2014), the temporal evolution is modelled as a probabilistic Markov model of the transition dynamics. The state vector of cluster probabilities may initially start in a single centroid but eventually diffuses to a fixed point representing the post-transient attractor. This fixed point is well reproduced by CROM. In addition, CROM has provided valuable physical insights for the mixing layer and Ahmed body wake (Kaiser *et al.* 2014), for the turbulent boundary layer (Ishar *et al.* 2019), for combustion related mixing (Cao *et al.* 2014), and for control design (Kaiser *et al.* 2017; Nair *et al.* 2019).

A challenge for CROM is the temporal evolution: the state may quickly diffuse over the whole attractor, often within one typical time period. This study aims at cluster-based model with improved dynamics resolution following Fernex *et al.* (2019). The dynamics is modelled by ‘constant velocity flights’ between the centroids as ‘airports’. The transition probabilities and times are consistent with the snapshot data. The dynamics is thus restricted to a sparse network of routes between the centroids. Network models are enjoying increasing popularity in all fields of mathematical modeling including biology, sociology, computer sciences. Network models have been also employed to explain vortex dynamics (Nair & Taira 2015; Taira *et al.* 2016). Newman (2010) provides an excellent introduction to networks.

The paper is organized as follows. § 2 elaborates the methodology of cluster-based network model (CNM). The limit cycle dynamics and Lorenz attractor are employed as illustrating examples. § 3 describes the incompressible mixing layer configuration and outlines the direct numerical simulation. In § 4, CNM is benchmarked against the cluster-based Markov model (CMM). § 5 summarizes this study and outlines future directions of research.

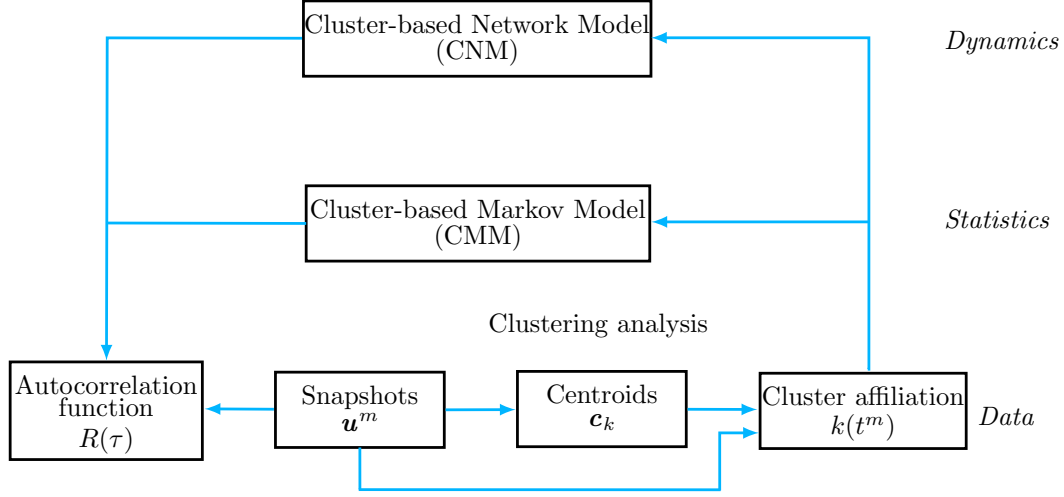


Figure 1: Principle sketch of cluster-based modeling. The time-resolved snapshots are partitioned into a predetermined number of clusters represented by centroids in an unsupervised manner. Thereafter, each snapshot has a cluster-affiliation  $k(t^m)$  being the index of the closest centroid. Cluster-based Markov models (CMM) describe the evolution of the population of these clusters. The solution of CMM quickly converges against the asymptotic probability distribution. The proposed cluster-based network model (CNM) resolves the dynamic transitions between the clusters by a deterministic-stochastic network.

## 2. Cluster-based modeling

In this section, we propose a novel cluster-based reduced-order model (ROM) for the coherent structure dynamics starting at the time-resolved snapshots. In § 2.1 and § 2.2 clustering and cluster-based Markov models (CMM) are recapitulated. Section 2.3 proposes a novel data-driven dynamic network resolving the transition dynamics between the clusters. In § 2.4, the time-discrete cluster-based ROM is enhanced for a continuous-time velocity prediction. The model validation includes the autocorrelation function of the flow as discussed in § 2.5. Figure 1 previews the methodology and will be explained later in the section. The relative advantages of CMM and CNM are illustrated for the Lorenz attractor in § 2.6.

### 2.1. Clustering as coarse-graining

We consider velocity fields in a steady domain  $\Omega$  which may be obtained from experiments or from numerical simulations. Starting point is an ensemble of  $M$  statistically representative, time-resolved snapshots as employed for Cluster-based Reduced-Order Modeling (CROM) (Kaiser *et al.* 2014), Dynamic Mode Decomposition (DMD) (Rowley *et al.* 2009; Schmid 2010) or Proper Orthogonal Decomposition (POD) (see, e.g., Holmes *et al.* 2012). The velocity field is equidistantly sampled with time step  $\Delta t$ , i.e. the  $m$ -th instant reads  $t^m = m\Delta t$ . The corresponding snapshot velocity field is denoted by  $\mathbf{u}^m(\mathbf{x}) := \mathbf{u}(\mathbf{x}, t^m)$ ,  $m = 1, \dots, M$ .

In CROM, the  $M$  snapshots  $\mathbf{u}^m(\mathbf{x})$  are coarse-grained into  $K$  clusters represented by the centroids  $\mathbf{c}_k(\mathbf{x})$ ,  $k = 1, \dots, K$  using the unsupervised k-means++ algorithm (Steinhaus 1956; MacQueen 1967; Lloyd 1982). The corresponding cluster-affiliation function maps a velocity field  $\mathbf{u}$  to the index of the closest centroid,

$$k(\mathbf{u}) = \arg \min_i \|\mathbf{u} - \mathbf{c}_i\|_{\Omega}. \quad (2.1)$$

This function defines cluster regions as Voronoi cells around the centroids

$$\mathcal{C}_i = \{\mathbf{u} \in \mathcal{L}^2(\Omega) : k(\mathbf{u}) = i\}. \quad (2.2)$$

This function can also be employed to map a snapshot index  $m$  to the representative cluster index  $k(m) := k(\mathbf{u}^m)$ . Alternatively, the characteristic function

$$\chi_i^m := \begin{cases} 1, & \text{if } i = k(m) \\ 0, & \text{otherwise} \end{cases} \quad (2.3)$$

describes if the  $m$ th snapshot is affiliated with the  $i$ th centroid. The latter two quantities are equivalent.

The performance of a set of centroids  $\{\mathbf{c}_k\}_{k=1}^K$  with respect to a given set of snapshots  $\{\mathbf{u}^m\}_{m=1}^M$  is measured by the average variance of the snapshots with respect to their closest centroid. The corresponding *inner-cluster variance* reads

$$J(\mathbf{c}_1, \dots, \mathbf{c}_K) = \frac{1}{M} \sum_{m=1}^M \|\mathbf{u}^m - \mathbf{c}_{k(m)}\|_{\Omega}^2. \quad (2.4)$$

The optimal centroids  $\{\mathbf{c}_k^*\}_{k=1}^K$  minimize this inner-cluster variance,

$$(\mathbf{c}_1^*, \dots, \mathbf{c}_K^*) = \arg \min_{\mathbf{c}_1, \dots, \mathbf{c}_K} J(\mathbf{c}_1, \dots, \mathbf{c}_K) \quad (2.5)$$

The argument is indeterminate with respect to a re-ordering. For CROM, we chose the first cluster as the one with the highest population, i.e. the largest number of associated snapshots. The  $(k+1)$ th cluster,  $k > 1$ , has the largest transition probability from the  $k$ th one.

The optimization problem (2.5) is solved by the k-means++ algorithm. The  $K$  centroids are initialized randomly and then iterated until convergence is reached or when the variance  $J$  is small enough. k-means++ repeats the clustering process 30 times and take the best set of centroids.

The number of snapshots  $n_k$  in cluster  $k$  is given by

$$n_k = \sum_{m=1}^M \chi_k^m \quad (2.6)$$

The centroids are the mean velocity field of all snapshots in the corresponding cluster. In other words,

$$\mathbf{c}_k = \frac{1}{n_k} \sum_{\mathbf{u}^m \in \mathcal{C}_k} \mathbf{u}^m = \frac{1}{n_k} \sum_{m=1}^M \chi_k^m \mathbf{u}^m. \quad (2.7)$$

In the following centroid visualizations, we accentuate the vortical structures by displaying the fluctuations  $\mathbf{c}_k - \bar{\mathbf{u}}$  around the snapshot mean  $\bar{\mathbf{u}}$  and not the full velocity field  $\mathbf{c}_k$ .

## 2.2. Cluster-based Markov model (CMM)

We briefly recapitulate CMM by Kaiser *et al.* (2014) as our benchmark cluster-based reduced-order model. In CMM, the state variable is the cluster population  $\mathbf{p} = (p_1, \dots, p_K)^T$ , where  $p_i$  represents the probability to be in cluster  $i$  and the superscript T denotes the transpose. The transition between clusters in a given time step  $\Delta t^c$  is described by the transition matrix  $\mathbf{P} = (P_{ij}) \in \mathcal{R}^{K \times K}$ . The superscript ‘c’ refers to cluster-based model. Here,  $P_{ij}$  is the transition probability to move from cluster  $j$  to cluster  $i$ . Let  $\mathbf{p}^l$  be the

probability vector at time  $t^l = l\Delta t^c$ , then the change in one time step is described by

$$\mathbf{p}^{l+1} = \mathbf{P}\mathbf{p}^l \quad (2.8)$$

With increasing iterations, the iteration (2.8) converges to the asymptotic probability  $\mathbf{p}^\infty := \lim_{l \rightarrow \infty} \mathbf{p}^l$ . In a typical case, (2.8) has a single fixed point  $\mathbf{p}^\infty$ . For completeness, a continuous form of Markov models with new transition matrix  $\mathbf{P}^c$  is mentioned:

$$\frac{d\mathbf{p}}{dt} = \mathbf{P}^c \mathbf{p}. \quad (2.9)$$

From the time-continuous form (2.9), the time-discrete one (2.8) can be derived. The opposite is not generally true. In the following, no continuous Markov models are employed.

A CMM of the time-resolved snapshots starts with cluster affiliation (2.1) which can also be considered function of time  $k(t)$ . We refer to the original paper for the determination of  $P_{ij}$  from  $k(t)$ . The time step  $\Delta t^c$  is a critical design parameter for CMM. A good choice is a value where the transition from one cluster to the next is likely. If the time step is too small, the Markov model idles many times in each cluster for a stochastic number of times before transitioning to the next cluster. The model-based transition time may thus significantly deviate from the deterministic data-driven trajectories through the clusters. If the time step is too large, one may miss intermediate clusters. We choose  $\Delta t^c = T/10$ , where  $T$  is the characteristic period of the flow. On a circular limit cycle with uniform rotation, this value is optimal for  $K = 10$  clusters, enforcing the transition from one cluster to the next in each time step.

In figure 2 (left column), the effect of the suboptimal time step is illustrated for the CMM of a uniform rotation  $u_1 = \cos(2\pi t)$ ,  $u_2 = \sin(2\pi t)$ . Here, 4 clusters and a time step  $\Delta t^c = 1/16$  are chosen. The probability to stay in the cluster during one time step is  $P_{11} = P_{22} = P_{33} = P_{44} = 3/4$  and the transition probability to the next counter-clockwise neighbour is  $P_{14} = P_{21} = P_{32} = P_{43} = 1/4$ . Thus, the probability to stay in one cluster for  $l$  steps exponentially decays,  $P_{11}^l$ . In contrast, the uniform rotation commands that the state is exactly three time steps in one cluster before it leaves in the fourth step. This example motivates the proposed cluster-based reduced-order model, foreshadowed in figure 2 (right column) and explained in the following section.

### 2.3. Cluster-based network model (CNM)

For CMM, the time step  $\Delta t^c$  is, as mentioned, an important design parameter. This design parameter can be avoided by the new proposed *Cluster-based Network Model* (CNM). The key idea is to abandon the ‘stroboscopic’ view of CMM and focus on non-trivial transitions from cluster  $j$  to cluster  $i$ . These transitions are characterized by two parameters: the probability  $Q_{ij}$  and a time-scale  $T_{ij}$ . Evidently, no time-step is needed for the description and the assumption of a constant transition time is found to be much more aligned with shear flow modes than assuming an exponential decay of residence time. Moreover, it could be relaxed by assuming a probability distribution of transition times.

In the following, the transition probability and transition time are inferred from the cluster affiliation function  $k(t)$ . The continuous form is convenient for discussion. The time discrete affiliation function  $k(m)$  can be made continuous by taking the cluster of the snapshot which is closest in time,

$$k(t) = k \left( \arg \min_m |t - t_m| \right).$$

The  $n$ th transition time  $t_n$  of the cluster affiliation is recursively defined as the first

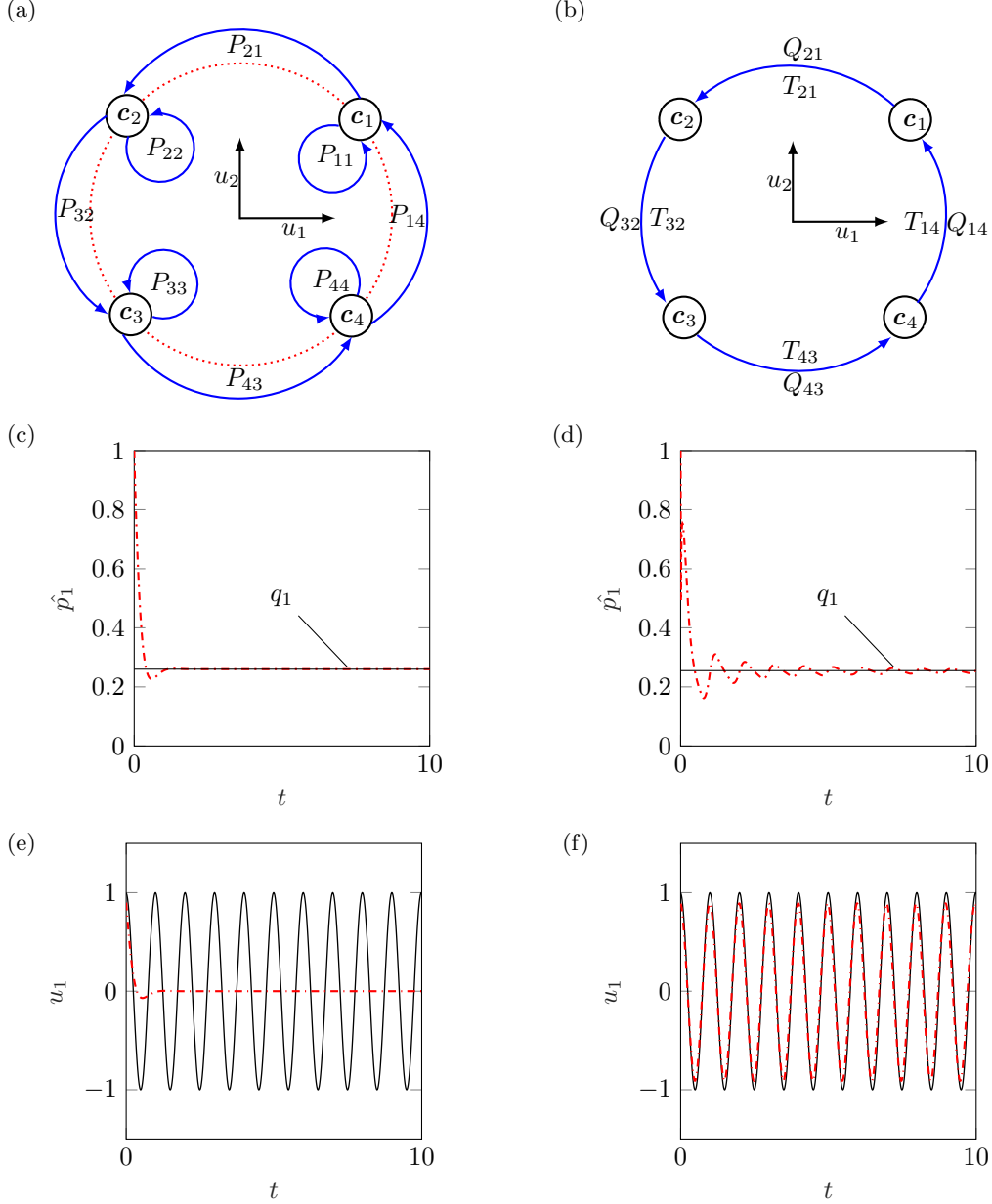


Figure 2: Introduction of cluster-based models for a limit cycle example. CMM and CNM are displayed in the left and right column, respectively. The uniform rotation  $u_1 = \cos(2\pi t)$ ,  $u_2 = \sin(2\pi t)$  in a two-dimensional plane is discretized by 4 centroids  $c_k$ ,  $k = 1, \dots, 4$ . (a) Phase portrait of CMM with time step  $\Delta t = 1/16$ . The centroids are near the limit cycle (red dashed line). The state vector residing in centroid  $c_i$  has the probability  $P_{ii}$  to stay in its state and  $P_{ji}$  to transition to centroid  $c_j$  in the considered time-step. (b) Phase portrait of the CNM. The state in centroid  $c_i$  moves uniformly to its counter-clockwise neighbour taking a quarter period  $T_{14} = T_{21} = T_{32} = T_{43} = 1/4$ . Here,  $Q_{14} = Q_{21} = Q_{32} = Q_{43} = 1$  and  $Q_{ij} = 0$  otherwise. The estimated probability evolution starting in cluster  $i = 1$  at  $t = 0$  is illustrated for CMM (c) and CNM (d). ((e)) and (f) present the model-based evolution of the first coordinate  $u_1$  for CMM and CNM, respectively. In (c)–(f), the solid black lines correspond to the uniform rotation and the dashed red line to the model.

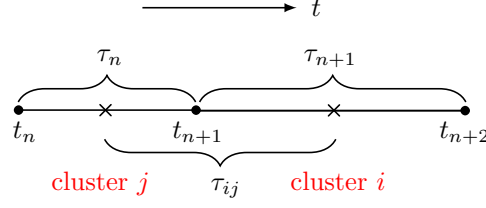


Figure 3: Sketch of times and periods employed in the cluster-based network model.  $\times$  marks the center of the cluster residence time, while  $\bullet$  denotes the transition between clusters.

discontinuity of  $k(t)$  for  $t > t_{n-1}$ . Here,  $t_0 = -\infty$ . The transition time  $t_n$  satisfies

$$k(t_n - \varepsilon) \neq k(t_n + \varepsilon) \quad (2.10)$$

for any sufficiently small positive  $\varepsilon$ . For  $t \in (t_n, t_{n+1})$ , the data-based trajectory is assumed to stay in cluster  $k$  at the averaged time  $(t_{n+1} + t_n)/2$  (see figure 3). The residence time in this cluster is defined by

$$\tau_n := t_{n+1} - t_n. \quad (2.11)$$

Let  $j$  and  $i$  be the indices of the clusters after  $t_n$  and  $t_{n+1}$  respectively. Then the transition time from  $j$  to  $i$  is defined as half of the residence time of both clusters,

$$\tau_{ij} := \frac{\tau_n + \tau_{n+1}}{2} = \frac{t_{n+2} - t_n}{2}. \quad (2.12)$$

This definition may appear arbitrary but is the least-biased guess consistent with the available data. The sum of all residence times from a given data set add up to the total investigated time period  $T_0$ .

The direct transition probability  $Q_{ij}$  and transition time  $T_{ij}$  can be inferred from the data. Then,

$$Q_{ij} = \frac{n_{ij}}{n_j}, i, j = 1, \dots, K; \quad (2.13)$$

where  $n_{ij}$  is the number of transitions from  $\mathbf{c}_j$  to  $\mathbf{c}_i$  and  $n_j$  the number of transitions departing from  $\mathbf{c}_j$  regardless of the destination point,

$$n_j = \sum_{i=1}^K n_{ij}, i, j = 1, \dots, K. \quad (2.14)$$

We emphasize that  $n_{ii} = 0$  for  $i = 1, \dots, K$  by very definition of a direct transition. The *direct transition matrix* (DTM)  $\mathbf{Q} = (Q_{ij}) \in \mathcal{R}^{K \times K}$  lumps these probabilities into a single entity.

Similarly, the direct transition time  $T_{ij}$  from cluster  $j$  to cluster  $i$  is taken to be the average from all values. This average is symbolically denoted by

$$T_{ij} = \langle \tau_{ij} \rangle \quad (2.15)$$

These values are lumped into the matrix  $\mathbf{T} = (T_{ij}) \in \mathcal{R}^{K \times K}$ .

It should be noted that a given trajectory may pass repeatedly through the same clusters (Voronoi cells) with different residence and transition times. With enough data this variability may be incorporated into the model. Our goal is to compare the Markov model with the most simple network model where constant (averaged) transition times are assumed.

CNM predicts the asymptotic cluster probability  $p_i^\infty$  in cluster  $i$ . Let  $[0, T_0]$  be a

sufficiently long time horizon simulated by the model. Then, the probability to stay in cluster  $i$  is the cumulative residence time normalized by the simulation time,

$$p_i^\infty = \frac{\sum \tau_i}{T_0}. \quad (2.16)$$

We return to introductory example depicted in figure 2. The CNM is seen to accurately describe the uniform rotation (subfigure f) and correctly yields the asymptotic cluster probability  $p_i^\infty = 1/4$ ,  $i = 1, \dots, 4$ . In contrast, the prediction horizon of the CMM is limited to roughly one period. After this time, the initial condition is forgotten and the asymptotic distribution is reached—rendering CMM unsuitable for dynamic prediction. However, CMM predicts the asymptotic state faster than the CNM. For this particular example, the CMM could be made equivalent to the CNM by choosing  $\Delta t^c = 1/4$ . However, the Markov model will inevitably diffuse the state with a range of cluster-transition times, e.g. for non-uniform rotation or more complex dynamics.

#### 2.4. Velocity fields associated with the cluster-based reduced-order models

The CMM describes the cluster population

$$\mathbf{p} = (p_1, \dots, p_K)^T \quad (2.17)$$

at discrete times  $t = l\Delta t^c$ . In the following, this population is considered to be continuous in time, e.g. by using linear or higher-order interpolation. The corresponding velocity field  $\mathbf{u}(\mathbf{x}, t)$  at time  $t$  is defined as the expectation value,

$$\mathbf{u}(\mathbf{x}, t) = \sum_{i=1}^K p_i(t) \mathbf{c}_i(\mathbf{x}) \quad (2.18)$$

where  $\mathbf{c}_i$  is the  $i$ th centroid.

The CNM is based on centroid visits at discrete times. The clusters  $k_0, k_1, k_2, \dots$  are visited at times

$$t_0 = 0, \quad t_1 = T_{k_1 k_0}, \quad t_2 = t_1 + T_{k_2 k_1}, \dots \quad (2.19)$$

consistent with the direct transition matrix  $(Q_{ij})$  and the transition times  $T_{ij}$ . A uniform motion is assumed between these visits. In other words, for  $t \in [t_n, t_{n+1}]$  the velocity field reads

$$\mathbf{u}(\mathbf{x}, t) = \alpha_n(t) \mathbf{c}_{k_n}(\mathbf{x}) + [1 - \alpha_n(t)] \mathbf{c}_{k_{n+1}}(\mathbf{x}), \quad \alpha_n = \frac{t_{n+1} - t}{t_{n+1} - t_n}. \quad (2.20)$$

We note that a smoother motion may be achieved with splines.

The actual flow computations are based on a lossless proper orthogonal decomposition (POD), as elaborated in the appendix A. The interpolations are performed with the mode amplitudes  $\mathbf{a} = (a_1, \dots, a_N)$  before transcribed into velocity fields via the POD expansion.

#### 2.5. Validation of the cluster-based reduced-order models

Following Protas *et al.* (2015), the cluster-based model is validated based on the computed and predicted autocorrelation function of the velocity field. The unbiased autocorrelation function reads

$$R(\tau) := \frac{1}{T - \tau} \int_\tau^T \langle \mathbf{u}(\mathbf{x}, t - \tau) \cdot \mathbf{u}(\mathbf{x}, t) \rangle_\Omega dt, \quad \tau \in [0, T]. \quad (2.21)$$



This function reveals the turbulent fluctuation level  $R(0)$  and the frequency spectrum. Moreover, the problem of comparing two trajectories with finite dynamic prediction horizons due to increasing phase mismatch is avoided (Pastoor *et al.* 2005).

In case of the CNM, the modeled autocorrelation function  $\hat{R}$  is based on the modelled velocity field (2.20). In case of the CMM, the time integration quickly leads to the average flow and is not indicative for the range of possible initial conditions. Hence,  $K$  trajectories are considered starting with  $p_k = 1$  for each cluster  $k$ , or, equivalently,  $\mathbf{p}(t = 0) = (\delta_{1k}, \dots, \delta_{Kk})$ . These cluster-specific autocorrelation functions are weighted with the cluster probability  $p_i^\infty$

$$\hat{R}(\tau) := \sum_{k=1}^K p_i^\infty \int_0^T \langle \mathbf{u}(\mathbf{x}, t) \cdot \mathbf{u}(\mathbf{x}, t + \tau) \rangle_\Omega dt, \quad \tau \in [0, T]. \quad (2.22)$$

### 2.6. Lorenz system as an illustrating example

Following the original CMM paper by Kaiser *et al.* (2014), the CNM is illustrated for the celebrated Lorenz (1963) system, arguably the first demonstration of chaotic dynamics in low-dimensional dynamics. The Lorenz system is a three-dimensional autonomous system of nonlinear ordinary differential equations. The derivation was inspired by a Galerkin model of Rayleigh-Benard convection, but typical selected parameters clearly exceed the range of model validity Sparrow (1982). The system features non-periodic, deterministic, dissipative dynamics associated with exponential divergence and convergence to a fractal strange attractor. The three coupled nonlinear differential equations read

$$\frac{dx}{dt} = \sigma(y - x) \quad (2.23a)$$

$$\frac{dy}{dt} = x(r - z) - y \quad (2.23b)$$

$$\frac{dz}{dt} = xy - bz \quad (2.23c)$$

with the system parameters  $\sigma = 10$ ,  $b = 8/3$  and  $r = 28$ . For these parameters, there are three unstable fixed points at  $(0, 0, 0)$  and  $(\pm\sqrt{72}, \pm\sqrt{72}, 27)$ , denoted by  $F^+$  and  $F^-$ , respectively. The attractor of Lorenz system resembles two butterfly wing around  $F^+$  and  $F^-$  in phase space. The trajectory typically oscillates for several periods with increasing amplitude around a fixed point ( $F^+$  or  $F^-$ ) before it moves to the other wing. The number of revolutions made on either side varies unpredictably from one cycle to the next.

The Lorenz equations (2.23) are solved employing an explicit fourth-order Runge-Kutta scheme with an initial condition on the attractor. The time-resolved snapshots data  $\mathbf{x}(t_m)$  with  $\mathbf{x} = [x, y, z]$  are collected at a sampling time step  $\Delta t = 0.005$  corresponding roughly one thousands of a typical oscillation period. The k-means ++ algorithm partitions  $M = 1,000,000$  snapshots into  $K = 10$  clusters. Figure 4(a) displays a phase portrait of the corresponding clusters. The snapshots associated with one cluster are highlighted by the same color. The 10 clusters feature three different subsets: the transition clusters  $k = 1, 2$  between two butterfly wings, the  $F^-$  wing related cluster  $k = 3, 4, 5, 6$  and clusters  $k = 7, 8, 9, 10$  associated with the  $F^+$  wing. The wing-related cluster groups represent approximately  $90^\circ$  phase bins and don't resolve the amplitude. Evidently, the 10 clusters are a coarse representations of the state.

In the following, the dynamics are resolved by the network model of § 2.3. The 10 centroids are considered as nodes in the network. The transition between these centroids define directed edges characterised by direct transition matrix  $\mathbf{Q}$  and the flight times

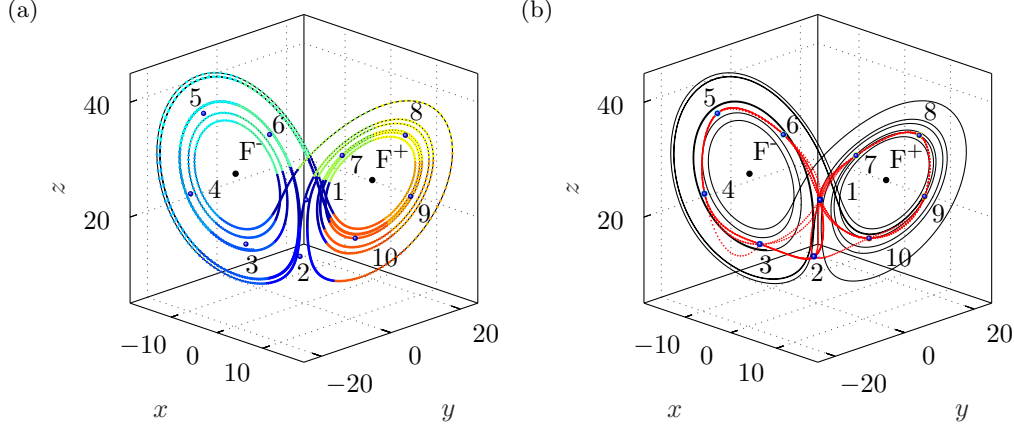


Figure 4: Cluster-based network modeling for the Lorenz attractor. (a) Cluster partitioning: The centroids are displayed as colored solid circles. A trajectory is illustrated by a black curve. The dots on this trajectory are colored according to their cluster affiliation. The clusters  $k = 3, 4, 5, 6$  oscillate around the fixed point  $F^-$  and clusters  $k = 7, 8, 9, 10$  around  $F^+$ . The clusters  $k = 1, 2$  connect both ‘ears’ of the Lorenz attractor. (b) The trajectory of the CNM (red dashed line). The centroids represent the network nodes and edges represent possible transitions. Here, trajectory of CNM is obtained by a spline-interpolation through the visited centroids.

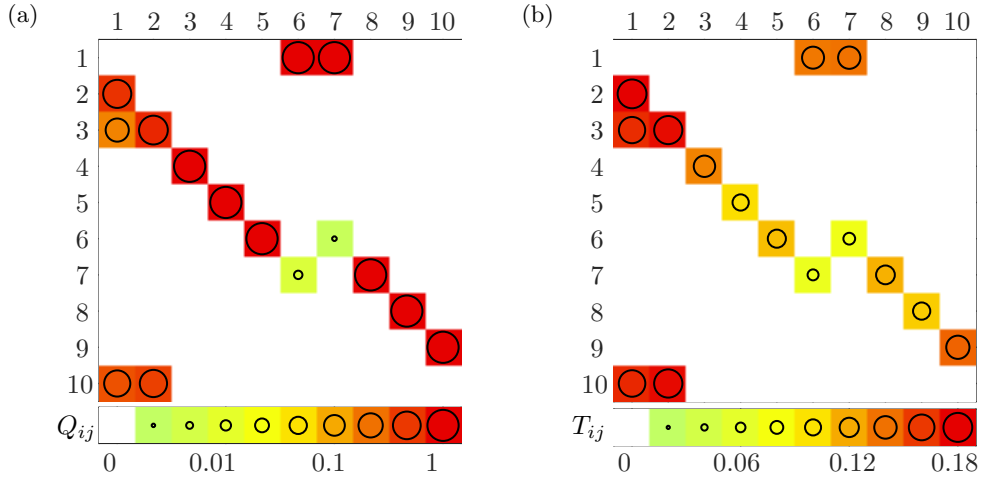


Figure 5: Cluster-based network model for the Lorenz attractor. (a) Direct transition matrix ( $Q_{ij}$ ) (b) Transition time ( $T_{ij}$ ).

$\mathbf{T}$ . The connectivity is described by the adjacency matrix  $H(\mathbf{Q})$  where  $H$  denotes the Heaviside function: non-vanishing elements of  $\mathbf{Q}$  are replaced by unity (Newman 2010). Figure 5, displays the DTM  $\mathbf{Q}$  (subfigure (a)) and associated transition time matrix  $\mathbf{T}$  (subfigure (b)). The matrices reveal three distinct cluster groups consistent with the phase diagram of figure 4. Clusters 1 and 2 allow transitions to 3 and 10, i.e. the  $F^-$  and  $F^+$  wing, respectively, and have been called *flipper clusters* by Kaiser *et al.* (2014). The cluster transition sequence  $3 \rightarrow 4 \rightarrow 5 \rightarrow 6 \rightarrow 1 \rightarrow 2 \rightarrow 3$  is the dominant cyclic group associated with the  $F^-$  wing. Another cyclic groups skips cluster 2:  $3 \rightarrow 4 \rightarrow 5 \rightarrow 6 \rightarrow 1 \rightarrow 3$ . A cyclic group through the  $F^+$  wing reads  $10 \rightarrow 9 \rightarrow 8 \rightarrow 7 \rightarrow 1 \rightarrow 10$ . A longer

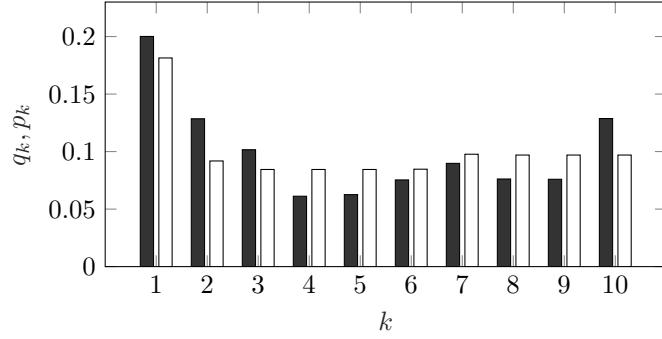


Figure 6: Cluster-based probability distribution of the Lorenz system (solid rectangles) and the corresponding CNM (open rectangles). The CNM results are based on 20,000 transitions.

sequence includes the 2nd cluster:  $10 \rightarrow 9 \rightarrow 8 \rightarrow 7 \rightarrow 1 \rightarrow 2 \rightarrow 10$ . The transition times in the wing centroids are noticeably smaller than the passage through the flipper clusters.

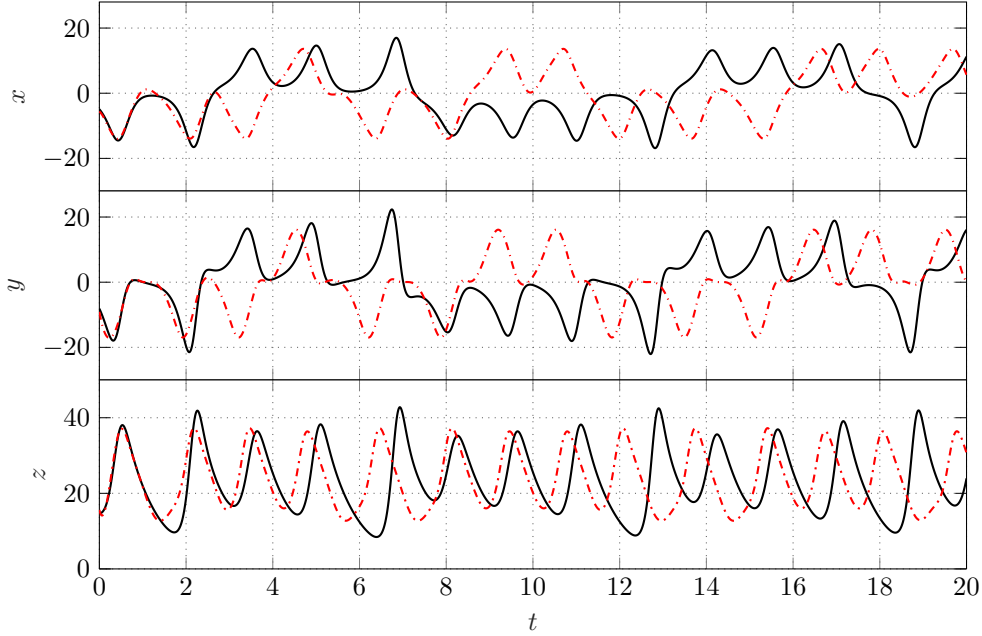


Figure 7: Evolution of the Lorenz system  $x, y, z, t \in [0, 20]$  from integrating the dynamical system (black solid line) and from the prediction of the CNM (red dashed line).

Figure 6 compares the asymptotic population  $\mathbf{p}^\infty$  predicted by CNM with the population from a long-term simulation. The CNM statistics are based on 20,000 transitions while the integration of the Lorenz equations is performed over 5000 time units. Both statistics correspond to roughly 800 periods found to be sufficient for an accurate statistics. The relative error of the CNM is up to approximately 10%. This error does not decrease with much larger integration times, but is linked to the coarse-graining of the state to Voronoi cells around the centroids. The assumed constant transition time  $\tau_{ij}$  for all trajectories from cluster  $j$  to cluster  $i$  is a crude assumption. In fact, the transition times

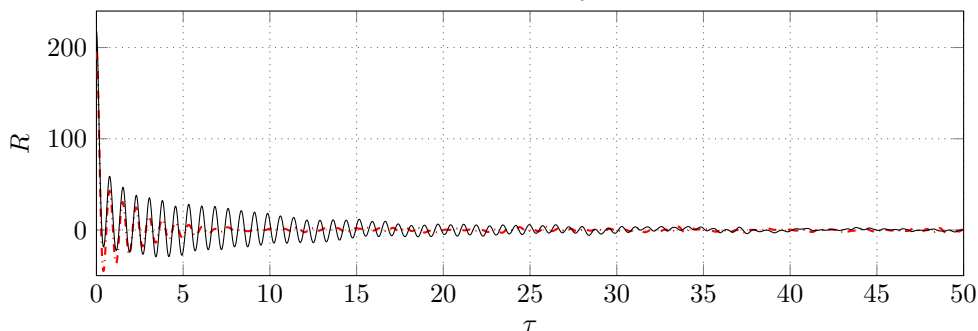


Figure 8: Autocorrelation function of the Lorenz system (black solid line) and the CNM (red dashed line).

can vary by a large factor and can thus give rise to significant systematic errors. A more accurate transition model may, for instance, include earlier transitions for a more realistic representation of the trajectory. Intriguingly, the CMM has an error of only 0.5% which is one order of magnitude lower. Due to the stroboscopic monitoring of the CMM states, no estimates of the transition times are required and one source of systematic errors is excluded by construction. A distinguishing feature of the CNM is the resolution of the temporal dynamics illustrated in figure 7. The evolution of the model-based trajectory is hardly distinguishable from the one obtained by numerical integration. Smoothness of the CNM trajectory has been achieved by splines connecting the states between two consecutive centroid visits. Yet, the oscillatory amplitude growth in both wings cannot be resolved with this low cluster-based resolution.

Finally, the autocorrelation of the simulation (black solid curve) and the CNM (red dashed curve) is presented for aggregate comparison in figure 8. CNM roughly reproduces the fast oscillatory decay of the autocorrelation function in the first five periods.

### 3. Flow Configuration

In this section, the numerical simulation of the incompressible mixing layer is described. The flow configuration of the mixing layer and the employed direct Navier-Stokes solver is described in § 3.1. In § 3.2, the dominant flow features of the mixing layer are presented.

#### 3.1. Mixing layer configuration and direct numerical simulation

The two-dimensional incompressible mixing layer with velocity ratio of 3:1 is considered as the test plant in this paper. The velocity ratio is a common choice in the literature (Comte *et al.* 1998; Noack *et al.* 2005; Kaiser *et al.* 2014). The low- and high-speed streams have velocities  $U_1$  and  $U_2$ , respectively. The convection velocity  $U_c$  of coherent structure is well approximated by the average velocity (Monkewitz 1988):

$$U_c = \frac{U_1 + U_2}{2}. \quad (3.1)$$

The initial vorticity thickness is denoted by  $\delta_0$ . The Newtonian fluid is characterized by the density  $\rho$  and kinematic viscosity  $\nu$ . The flow characteristics are described by the Reynolds number based on the convection velocity  $Re = U_c \delta_0 / \nu$  and velocity ratio. In the sequel, all quantities are assumed to be non-dimensionalized with the initial vorticity thickness  $\delta_0$ , the low-speed velocity  $U_1$  and the density  $\rho$ .

The flow is described in a Cartesian coordinate system  $(x, y)$  with the origin at maximum gradient location of the inlet profile. The  $x$ -axis points in streamwise direction and

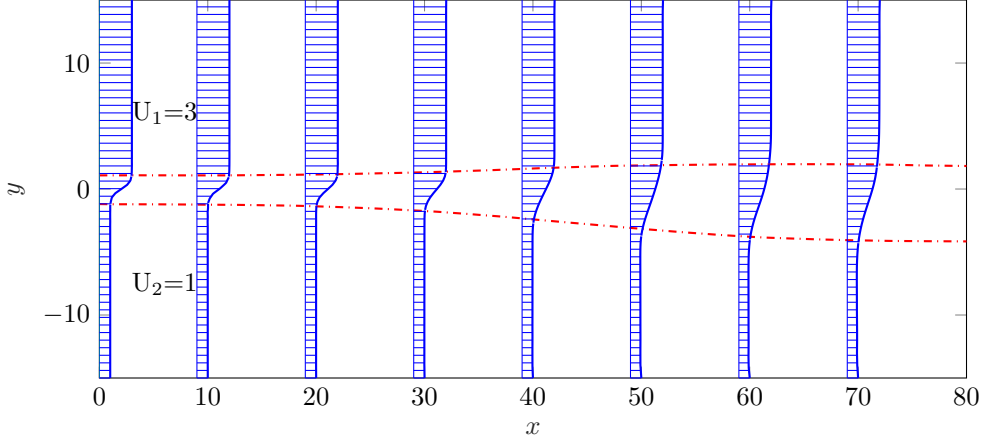


Figure 9: Numerical simulation sketch of incompressible mixing layer. An unperturbed tanh velocity profile  $u(y) = 2 + \tanh(2y)$  is patched in the inlet of a rectangular domain. Time-averaged streamwise velocity profiles separated by  $\Delta x=10$  are visualized by blue lines. The red dashed curves mark the mixing layer thickness, We chose the 90% thickness of the profile starting with the average velocity, i.e.,  $u = 2.9$  and  $u = 1.1$ .

the  $y$ -axis points in the direction of the high-speed stream. The velocity components in  $x$ - and  $y$ -direction are denoted by  $u$  and  $v$  respectively.

Figure 9 describes the rectangular computational domain

$$\Omega := \{(x, y) \in \mathcal{R}^2 : 0 \leq x \leq 80 \wedge |y| \leq 15\} \quad (3.2)$$

with 10237 nodes and 2248 triangular elements. The location vector is denoted by  $\mathbf{x} = (x, y)$ . Similarly, the velocity vector is denoted by  $\mathbf{u} = (u, v)$ . The inlet velocity profile reads

$$u = 2 + \tanh\left(\frac{2y}{\delta_0}\right), \quad v = 0, \quad \text{where} \quad \delta_0 = 1. \quad (3.3)$$

The Kelvin-Helmholtz vortices are triggered at the inlet by a stochastic perturbation of the  $u$ -component for  $y \in [-2, 2]$  with a standard deviation of  $0.01U_c$ .

The streamwise extend of the domain is 80. This corresponds to a downwash time of 40 given the convection velocity of 2. This is the minimum time for the transient time as all initial interior vortices will leave the domain. A simulation over 400 convective units corresponds to 10 downwash times. This period is found to be sufficient for a good statistics of the mean value and fluctuation level. One simulation yields  $M = 10,000$  velocity snapshots  $\mathbf{u}^m(\mathbf{x}) = \mathbf{u}(\mathbf{x}, t^m)$ , where the sampling times  $t^m = 0.04 m$  start with  $t = 0$  in the converged post-transient phase. The sampling frequency 25 is two orders of magnitude larger than the dominant shear-layer frequency of  $f = 0.1075$  in the most active downstream region.

An in-house direct numerical simulation solver was employed to simulate the incompressible mixing layer. This solver is based on the Finite-Element Method (FEM) with third-order Taylor-Hood elements with implicit third-order time integration. The solver has been used for numerous configurations, like the cylinder wake (Noack *et al.* 2016), the mixing layer (Shaqarin *et al.* 2018), the fluidic pinball (Ishar *et al.* 2019), to name only a few.

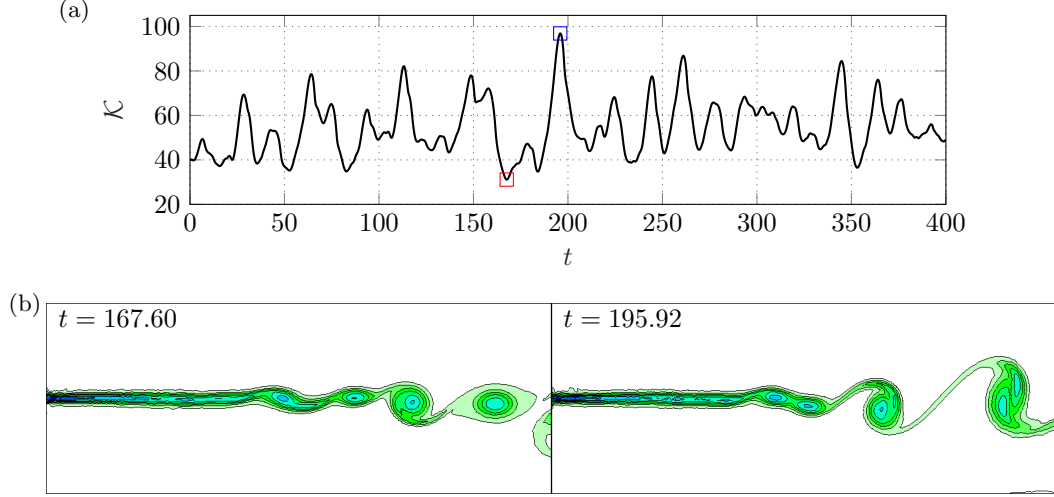


Figure 10: Mixing layer simulation. (a) Energy fluctuation over time with the maximum marked by a blue square and minimum by a red square. (b) Vorticity fields associated with the maximum and minimum fluctuation energy. The minimum (left) corresponds to a K-H vortex at  $t = 167.60$ . The maximum (right) features vortex pairing at  $t = 195.92$ . The curves represent isolines of vorticity. Higher values corresponds to darker green areas.

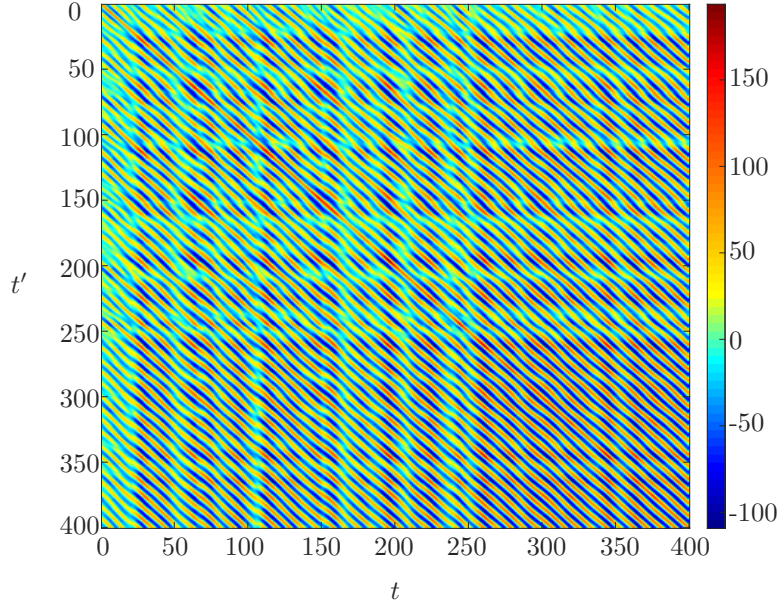


Figure 11: Autocorrelation matrix (3.4) of the mixing layer for  $t \in [0, 400]$ . The value is presented in the colorbar. The plot is based on 401 snapshots collected at uniform time steps  $\Delta t = 1$ .

### 3.2. Flow features

The incompressible mixing layer exhibits two typical behaviours. First, the initial dynamics is characterized by the roll-up of vorticity originating from the Kelvin-Helmholtz (K-H) instability (see left in figure 10(a)). Second, these vortices pair further downstream

as can be seen at the outlet region of figure 10(b). This vortex pairing contributes to the mixing layer growth. The location of vortex pairing may change significantly in time. Upstream (downstream) vortex pairing is associated with high (low) fluctuation energy.

The time-averaged velocity field in figure 9 shows the mixing layer growth. The velocity thickness is visualized by red solid line and is defined as the distance between transverse locations where the mean streamwise velocity was equal to  $U_1 - 0.1\Delta U$  and  $U_2 + 0.1\Delta U$ . The mixing layer thickness increases significantly between  $x = 30$  and  $x = 60$ . Here, vortex pairing leads to this thickness increase.

The temporal dynamics may be inferred from the evolution of the fluctuation energy in figure 10. The fluctuations indicate narrow bandwidth oscillatory behaviour. More refined insights may be gained from the correlation function between the flows at time  $t$  and  $t'$ ,

$$C(t, t') = \int_{\Omega} d\mathbf{x} \mathbf{u}'(\mathbf{x}, t) \cdot \mathbf{u}'(\mathbf{x}, t') \quad (3.4)$$

Figure 11 illustrates the autocorrelation function for  $t, t' \in [0, 400]$ . The fluctuation energy of figure 10(a) is quantified in the diagonal,  $\mathcal{K}(t) = C(t, t)/2$ . The wavy pattern indicates oscillatory coherent structures. The changes from pure periodicity are caused by vortex pairing at a large range of streamwise locations.

#### 4. Cluster-based reduced-order modeling of the mixing layer

In this section, the cluster-based models are applied to a two-dimensional incompressible mixing layer with Kelvin-Helmholtz vortices undergoing vortex pairing. First, the snapshots of incompressible mixing layer are coarse-grained into centroids in § 4.1. Following Kaiser *et al.* (2014), a cluster-based Markov model (CMM, § 4.2) is developed as benchmark for the proposed network model (CNM, § 4.3).

##### 4.1. Clustering

Both reduced-order models are based on the direct numerical simulation of the two-dimensional incompressible mixing layer described in § 3.  $M = 10,000$  velocity field snapshots of the post-transient phase are sampled with a time step  $\Delta t = 0.04$ .

The computational load of clustering is significantly reduced by an effectively lossless POD compression detailed in Appendix A. In fact, all operations are performed on the POD amplitude vector  $\mathbf{a} = [a_1, a_2, \dots, a_N]^T$  instead of the snapshots.

The  $M$  snapshots are clustered with the k-means++ algorithm into  $K = 10$  centroids. This number is small enough to allow for the physical interpretation of all centroids and all transitions but large enough for a meaningful reduced-order model. Figure 12 illustrates the transverse velocity fluctuation of the centroids. The first 7 centroids show the streamwise convection of Kelvin-Helmholtz (K-H) vortices, while the next 3 centroids resolve a vortex pairing (VP) event. In centroid 8, two vortices merge at the beginning of the vortex chain. In the following 2 centroids, the merging is completed and leads to a large vortex. Note that the VP centroids  $k = 8, 9, 10$  have pronounced vortices at similar position as the KH centroids  $k = 4, 5, 6$ , respectively.

The centroids represent characteristic stages in the mixing layer dynamics as can be elucidated in a proximity map. This map reflects the configuration matrix  $\mathbf{D} = (D_{ij}) \in \mathcal{R}^{K \times K}$  comprising the distance between two centroids:

$$D_{ij}^c := \|\mathbf{c}_i - \mathbf{c}_j\|_{\Omega}, i, j = 1, 2, \dots, K. \quad (4.1)$$

Following Kaiser *et al.* (2014), the proximity map is used to represent the configuration

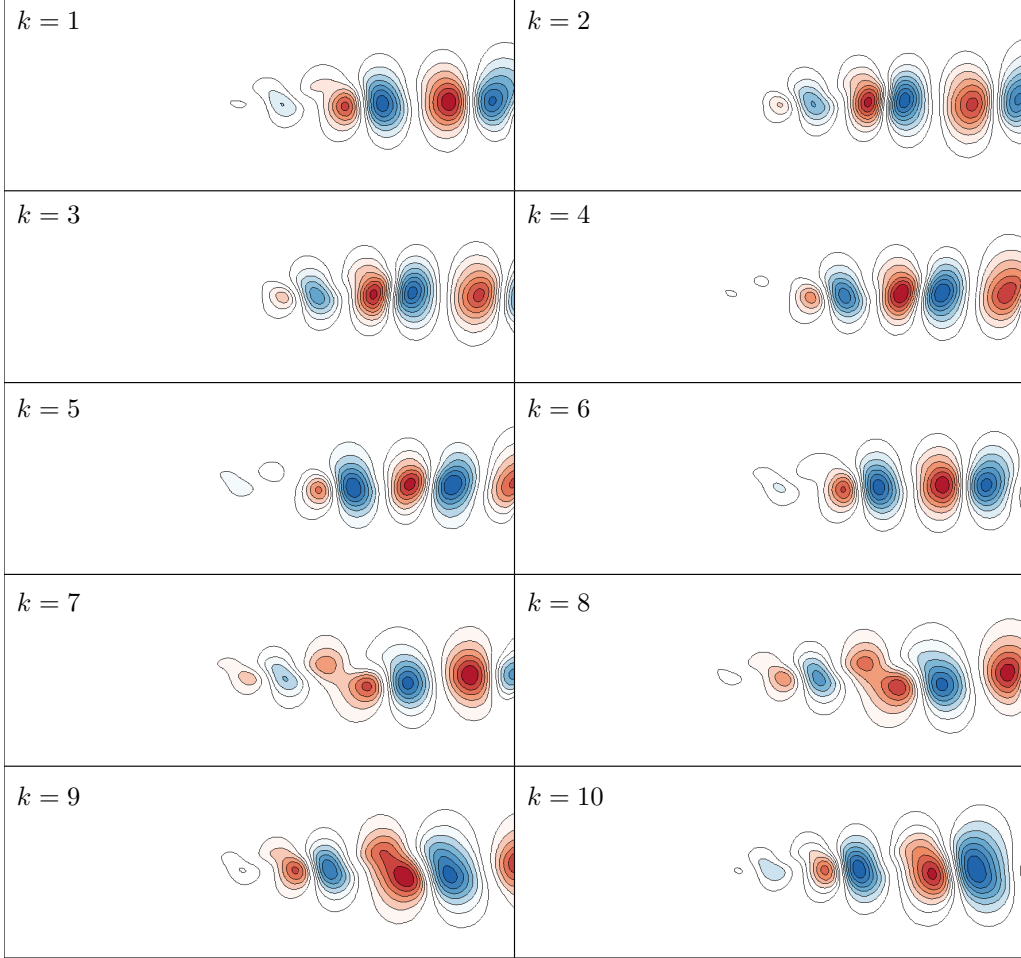


Figure 12: The cluster centroids  $\mathbf{c}_k$ ,  $k = 1, \dots, 10$ , of the mixing layer. The transverse velocity fluctuation is depicted with contour lines. Red and blue regions mark positive and negative values.

matrix  $\mathbf{D}$  in a two-dimension feature space  $\gamma \in \mathcal{R}^2$  optimally preserving the relative distances. The proximity map employs *Classical Multidimensional Scaling* (CMDs) (Mardia *et al.* 1979). Figure 13(a) displays centroids close to a circle which is characteristic for vortex shedding.

#### 4.2. Markov model

The temporal mixing-layer evolution is characterized by the cluster transition matrix  $\mathbf{P}$  illustrated in figure 13(b).  $P_{ij}$  represents the probability of moving from cluster  $j$  to  $i$  in one forward time step. Here, we choose a time step  $\Delta t^c = T/10 = 1$  where the  $T = 10$  is the dominant period of the evolved mixing layer.

The cluster transition matrix reveals two cyclic groups. The first group  $1 \rightarrow 2 \rightarrow 3 \rightarrow 4 \rightarrow 5 \rightarrow 6 \rightarrow 7 \rightarrow 1$  is consistent with the convection process of the K-H vortex shedding observed in the centroid visualization. This periodic process corresponds to a nearly uniform clockwise rotation in the proximity map. The second cyclic group  $8 \rightarrow 9 \rightarrow 10 \rightarrow 7 \rightarrow 1 \rightarrow 2 \rightarrow 8$  comprises VP centroids  $k = 8, 9, 10$  and shares two centroids



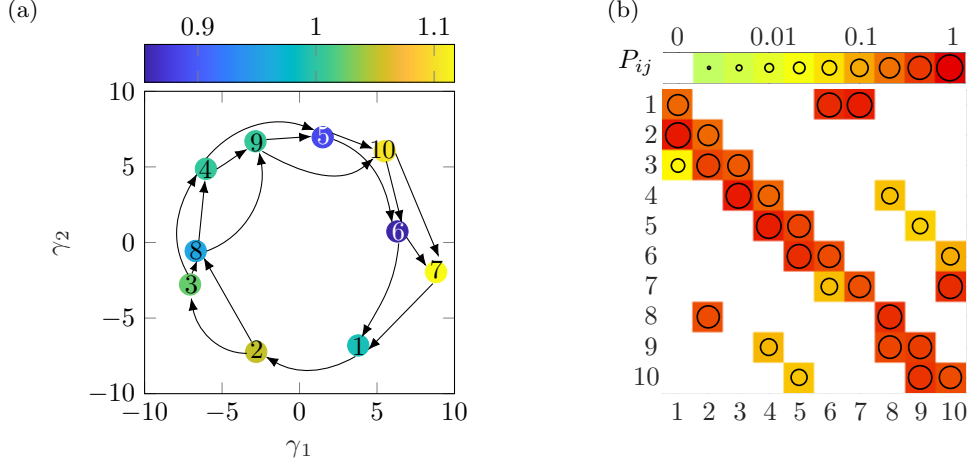


Figure 13: Cluster-based Markov model of the mixing layer. (a) Proximity map of centroids. Each centroid is marked by solid coloured circle. The color denotes the relative energy content (see colorbar on top). Unity corresponds to the average value. (b) Transition matrix. The probability value is displayed by the background color and the radius of responding circle.

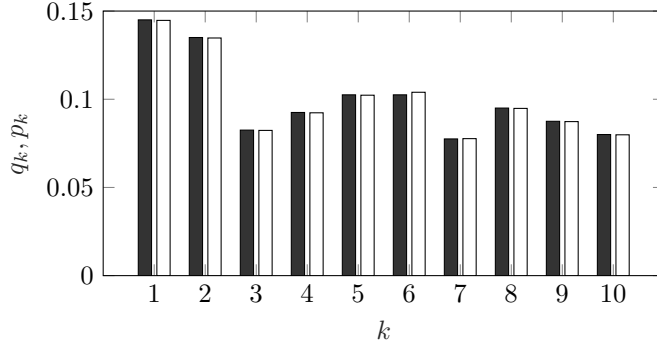


Figure 14: Cluster-based Markov model of the mixing layer. The figure shows the cluster probability distribution computed from affiliation  $k(t^m)$ . Solid rectangles denote the probability  $q_k$  from the DNS data. Open rectangles represent asymptotic values from CMM after  $l = 35$  iterations.

with the K-H regime. These dynamics also lead to a nearly uniform clockwise rotation in the feature space. There are also transitions from the VP to K-H regime, e.g.  $8 \rightarrow 4$ ,  $9 \rightarrow 5$ ,  $10 \rightarrow 6$  and  $10 \rightarrow 7$  and in the opposite direction. All these transitions are between similar centroids of both groups.

The evolution of the cluster population vector  $\mathbf{p}^l$  at  $t = l\Delta t^c$  is investigated by iterating equation (2.8). Figure 14 compares the probability distribution of DNS data and the model-based asymptotic vector  $\mathbf{p}^\infty$ . The agreement is astonishingly good for such a low-order model. The probability vector converges quickly to a unique, stationary probability distribution near  $t = 20$ .

In figure 15, the dynamics of CMM is illustrated for the first cluster probability  $p_1$  and the first POD mode amplitude  $a_1$  inferred from the flow state (2.18). Starting point is direct numerical simulation starting at  $t = 0$  close to the first cluster  $\mathbf{c}_1$  which corresponds to the probability vector  $\mathbf{p} = (1, 0, 0, 0, 0, 0, 0, 0, 0, 0)^T$ . The probability and POD mode

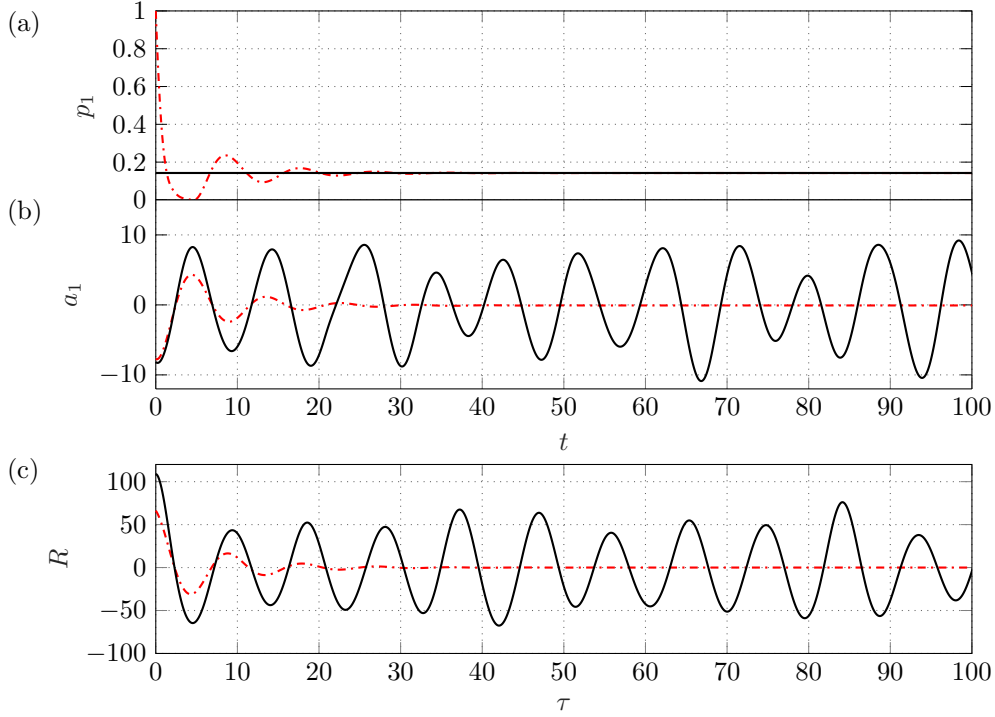


Figure 15: Dynamics of the cluster-based Markov model. (a) Probability evolution for DNS (black solid line) and for CMM (red dashed line). The probability of the first cluster  $p_1$  quickly converges to  $p_i^\infty$  around  $t = 35$ . The corresponding DNS value is 0.1325 and represented by a horizontal line. (b) The evolution of the first POD mode amplitude  $a_1$  for DNS (black solid line) and CMM (red dashed line). (c) The autocorrelation function for DNS (black solid line) and for CMM (red dashed line).

amplitude of CMM show a convergence after around  $l = 35$  iterations or, equivalently  $t \approx 35$ . The solid horizon line denotes  $q_1$ , i.e. the population of the first cluster from DNS data. The POD mode amplitude  $a_1$  performs three strongly damped oscillations before vanishing.

Figure 15c shows a oscillating quickly decaying autocorrelation function of CMM which is consistent with the observations for  $a_1$  and  $p_1$ . In contrast, the autocorrelation function associated with the DNS keeps oscillating around with an amplitude around 50% of the average fluctuation level. This level indicates that half of the fluctuation energy resides in repeating oscillatory flow structures while the other half is of non-repeating stochastic nature.

#### 4.3. Network model

In this section, a *Cluster-based Network Model* (CNM) is developed using the same snapshot data and same centroids. Starting point for the dynamic network is the cluster affiliation function  $k(t)$ . Following § 2.3, the direct cluster transition matrix  $\mathbf{Q}$  with associated average transition times  $\mathbf{T}$  are derived. Figure 16 illustrates both matrices. These matrices have the almost same structure as the Markov model except for the diagonal

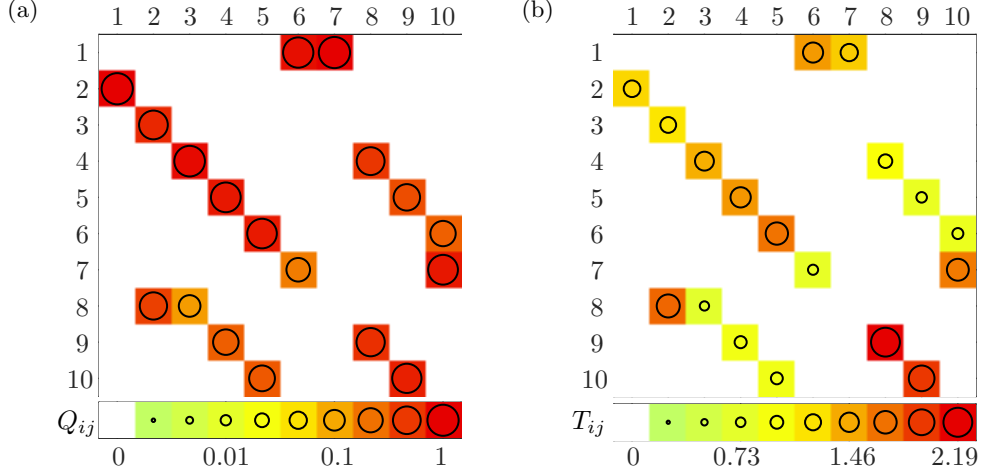


Figure 16: Dynamics of the cluster-based network model for the mixing layer. (a) Direct transition matrix. (b) Averaged transition time. The non-vanishing values are denoted by the circle radius and the colorcode from the bottom caption.

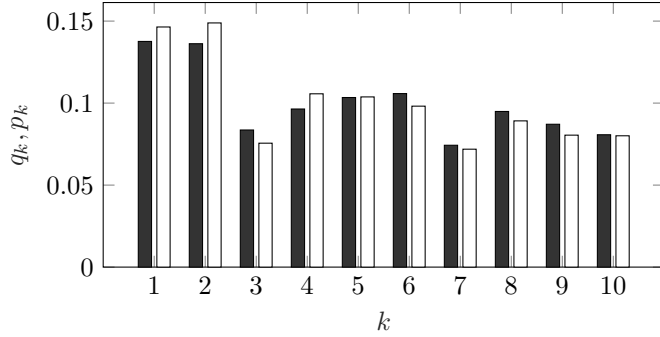


Figure 17: Probability distribution of the mixing layer from DNS (solid rectangle) and CNM (open rectangle). The CNM values are obtained from simulating 20,000 clusters transitions.

elements which are vanishing by design. In other words,

$$Q_{ii} = T_{ii} = 0 \quad \forall i \in \{1, \dots, K\}, \quad (4.2a)$$

$$H[P_{ij}] = H[Q_{ij}] = H[T_{ij}] \quad \forall i, j \in \{1, \dots, K\} \wedge i \neq j, \quad (4.2b)$$

$H$  being again the Heaviside function. Vanishing diagonal elements (4.2a) arise from the requirement of non-trivial transitions. Theoretically, the trajectory may terminate in a cluster, like in a stable fixed point of a linear dynamical system. This case is not compatible with the goal to model a well-resolved non-trivial attractor and shall be ignored in this study. Equation (4.2b) requires a sufficiently small time-step of the CMM. Otherwise, the stroboscopic view on the trajectory may miss a crossing of an intermediate cluster. This happens with the transition from  $1 \rightarrow 2 \rightarrow 3$  in one CMM time step  $\Delta t^c$ . Hence,  $P_{31} \neq 0$  while  $Q_{31} = 0$ . However, this is a rare event as indicated by the small value of  $Q_{31}$ .

An inspection of  $\mathbf{T}$  reveals that the transition time between K-H and VP centroids is relatively small. This is consistent with the closeness of the corresponding centroids in the proximity map (figure 13(a)). An exception is the transition between K-H centroid 2 to

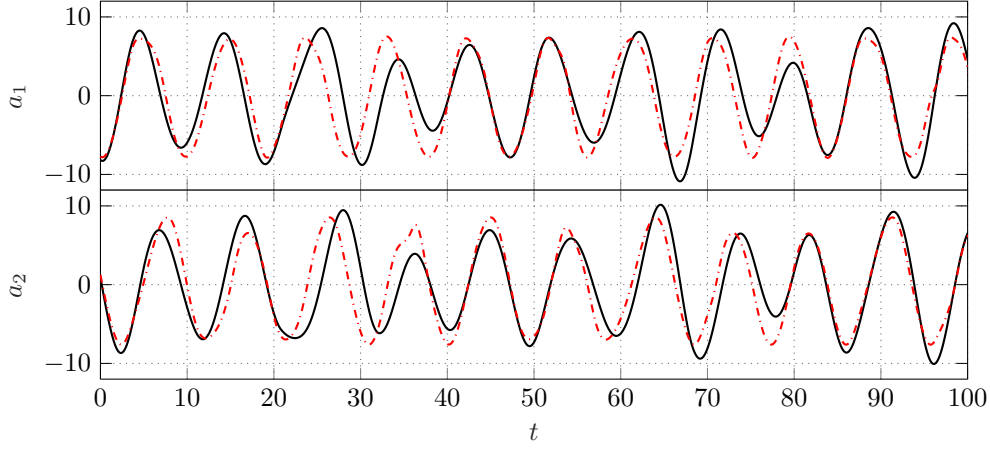


Figure 18: Evolution of mode amplitudes  $a_1$ ,  $a_2$  for the mixing layer  $t \in [0, 100]$ . The curves correspond to DNS (black solid line) and CNM (red dashed line).

VP centroid 8 which are well separated in the proximity map. Intriguingly, the transitions within the K-H and VP regime are also strongly correlated with the distances depicted in the proximity map. For instance, the smallest (largest) inner-regime transition from centroid 6 to 7 (8 to 9) is associated with a small (large) distance in the proximity map.

In the following, the temporal dynamics of CNM is investigated based on the identified centroids  $\mathbf{c}_k$ , the description of their connectivity DTM  $\mathbf{Q}$  and their flight times  $\mathbf{T}$ . Like a POD model, CNM is a grey-box model resolving the temporal dynamics and the associated coherent structures. We choose cluster  $k = 1$  as initial condition for DNS and for the CNM and integrate over  $l = 20,000$  transitions. In figure 17, the asymptotic cluster population  $\mathbf{p}^\infty$  from equation (2.16) is compared with  $\mathbf{q}$  from the DNS.

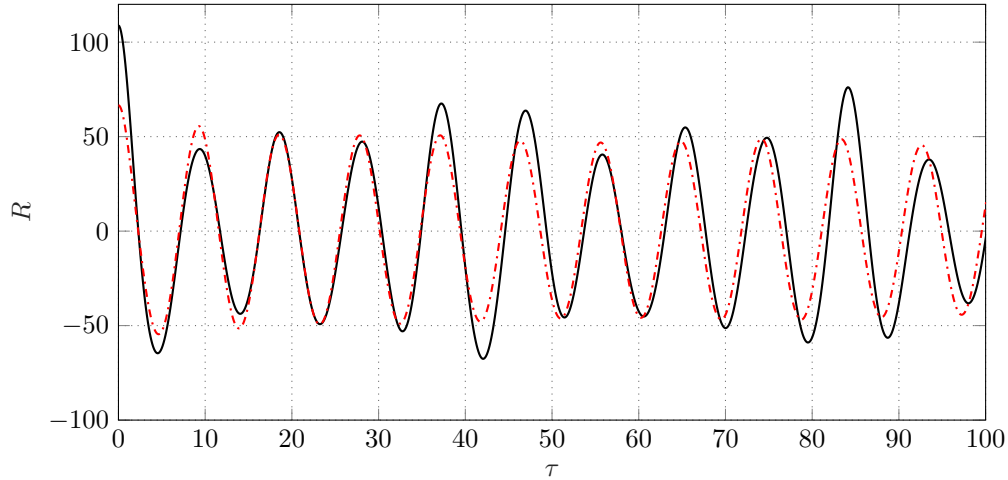


Figure 19: Autocorrelation function of the mixing layer for DNS (black solid line) and CNM (red dashed line).

Figure 18 shows the evolution of the first two POD mode amplitudes (red dashed curve). The CNM tracks well the amplitude and phase of the DNS over 100 time units.

Like for the Lorenz system, the temporal evolution is smoothed by a spline and does not use the non-smooth uniform motion between two consecutive centroid visits.

Figure 19 compares the autocorrelation function of the CNM and the DNS. Intriguingly, the model-based fluctuation level at vanishing time delay is significantly lower than the DNS value but becomes similar to oscillation level for arbitrary larger time horizon. The difference between DNS fluctuation level exhibited at vanishing time delay and the CNM-based one is the unresolved inner-cluster variance. The asymptotic fluctuation level represents coherent structures which are resolved by the chosen centroids and serve as coarse-grained recurrence points of the DNS. The good reproduction autocorrelation function is a posteriori justification for the chosen cluster number.

## 5. Conclusions

In the present study, we propose a new data-driven methodology for nonlinear dynamical systems. We trade compatibility with first principles, like with a POD-based Galerkin model, with simplicity and robustness of the modeling. Point of departure is the cluster-based Markov model (Kaiser *et al.* 2014) for time-resolved snapshot data. The snapshots are coarse-grained into few representative centroids. The temporal evolution of the state is conceptualized as straight constant velocity movement from one centroid to the next. The average flight time and the transition probabilities are inferred from the data. Thus, the dynamics is modeled by a deterministic-stochastic network model with the centroids as nodes, the straight trajectory segments as edges, the transition time as parameters of the edges and the transition probability characterizing the nodes.

The resulting cluster-based network model (CNM) has several desirable features: (1) The methodology is simple and automatable. (2) The off-line computational load is only slightly larger than a snapshot-based proper-orthogonal decomposition (POD). After the computation of the POD, the clustering and network model requires a tiny fraction of the computational operation. (3) The CNM has the same recurrence properties as the original data: If one cluster is visited multiple times in the data, it will also be a recurrence point of the CNM. (4) Long-term integration will never lead to a divergence—unlike POD models. (5) The framework is very flexible allowing, for instance, to incorporate multiple operating conditions.

The simplicity and robustness has a price. On the kinematic side, the vanilla version of CNM does not have the possibility to extrapolate the data, e.g., resolve oscillations at higher amplitudes not contained in the data. On the dynamic side, we lose the relationship to first principles: The network model is purely inferred from the snapshot data, without links to the Navier-Stokes equations. Subsequent generalizations need to overcome these restrictions.

CNM is applied to the Lorenz attractor. A k-means++ algorithm yields 10 centroids from a long time-resolved solution. 4 centroids represent each ear of the attractor and 2 the switching area. Despite the coarseness of the presentation, the temporal dynamics mimics well the oscillations in each ear and the switching between both ears. The agreement is mirrored by the similarity between the autocorrelation functions of the simulation and the CNM. Statistically, the cluster population is predicted with acceptable accuracy. The CNM dramatically outperforms the cluster-based Markov models (CMM) (Kaiser *et al.* 2014) in terms of predicting the temporal evolution. In contrast, CMM is more accurate for the cluster population. The error source of the CNM can be traced back to the chosen simple model of transition times.

The main demonstration of CNM is performed for a laminar two-dimensional mixing layer featuring Kelvin-Helmholtz (K-H) vortices and occasional vortex pairing. Again, the

snapshots are coarse-grained into 10 centroids. One group of centroids can be associated to K-H vortices and a second group to vortex pairing—similar to Kaiser *et al.* (2014). The CNM resolves well the temporal evolution of vortex formation and pairing, the fluctuation level, the autocorrelation function, and the cluster population.

CNM are found to have a distinct advantage over the departure point, CMM, namely the much longer prediction horizon as evidenced for the autocorrelation function. POD and DMD models may describe the same flow with similar number of modes (Protas *et al.* 2015). We emphasize that the construction of the CNM could be fully automated in a software package. In contrast, data-driven nonlinear Galerkin models may be designed as insightful least-order representations with interpretable modes. Moreover, the Galerkin dynamics may reveal the interplay between linear and nonlinear terms, as beautifully displayed in mean-field theory (Stuart 1971), self-consistent models (Mantič-Lugo *et al.* 2014), resolvent operator approaches (Gomez *et al.* 2016), finite-time thermodynamics (Noack *et al.* 2008) and criteria for boundedness (Schlegel & Noack 2015). Yet, a functional model requires the careful choice of flow data, potentially shift and other non-standard modes, subscale closure models and calibration techniques. Thus, cluster-based and POD based models have different niche applications.

CNM opens a novel automatable avenue for nonlinear dynamical modeling and provides a framework for estimation and model-based control (Fernex *et al.* 2019). The authors actively pursue this direction.

## Acknowledgements

Hao Li appreciates the Graduate Student Research Innovation Project of Hunan Province (Grant No. CX2018B027). He gratefully acknowledges the support of the China Scholarship Council (CSC) (No. CSC201803170267) during his study in Technische Universität Berlin and the excellent working conditions of the Hermann-Föttinger-Institute.

Jianguo Tan acknowledges the funding from the National Natural Science Foundation of China (No. 91441121).

B.R.N. thanks the French National Research Agency (ANR grant 'FlowCon'), the German Science Foundation (DFG, Collaborative Research Center 880 and grants SE 2504/2-1, SE 2504/3-1) and the Bernd Noack Cybernetics Foundation for additional support.

M.M. acknowledges partial funding from the Polish Ministry of Science and Higher Education (MNiSW) under the Grant No. 05/54/DSPB/6492.

We have highly profited from stimulating discussions with Marian Albers, Steven Brunton, Guy Yoslan Cornejo Maceda, Nan Deng, Arthur Ehlert, Eurika Kaiser, Matthew Lennie, Francois Lusseyran, Christian Navid Nayeri, Luc Pastur, Christian Oliver Paschereit, Wolfgang Schröder, Richard Semaan and Kunihiro Taira.

## Declaration of interests

The authors report no conflict of interest.

## Appendix A. Data compression for clustering

Clustering is a computationally expensive process based on a large number of area/volume integrals for the distance between snapshots and centroids. Let  $M$  and  $K$  be the amount of snapshots and clusters, respectively, then a single k-means iteration requires the computation of  $K \times M$  integrals. Let  $I$  be the number of k-means iterations and  $L$  be the

number of repetitions then the total number of integrals is  $L \times I \times K \times M$ . Typical values are  $K \sim 10$ ,  $I \sim 10K$  and  $L \sim 100$ .

The computational load can be significantly reduced by pre-processing the snapshot data with a lossless POD. The most expensive step of a typical snapshot POD is the computation of the correlation matrix with  $M \times (M + 1)/2$  area/volume integrals. Thus, the integral for the distance between two velocity fields transforms into the Euclidean norm with  $(M - 1)$ -dimensional vectors of POD mode amplitudes. The computational saving reads

$$\frac{M \times (M + 1)/2}{L \times I \times K \times M} = \frac{M + 1}{2L \times I \times K}. \quad (\text{A } 1)$$

With typical values, the savings are one or two orders of magnitudes.

For completeness and self-consistency, the snapshot POD algorithm is described. POD is performed with the whole computational domain  $\Omega$ . The inner product between two velocity fields  $\mathbf{v}(\mathbf{x})$ ,  $\mathbf{w}(\mathbf{x})$  in the square-integrable Hilbert space  $\mathcal{L}^2(\Omega)$  reads

$$(\mathbf{v}, \mathbf{w})_\Omega = \int_{\Omega} d\mathbf{x} \, \mathbf{v}(\mathbf{x}) \cdot \mathbf{w}(\mathbf{x}) \quad (\text{A } 2)$$

The corresponding norm is given by

$$\|\mathbf{v}\|_\Omega = \sqrt{(\mathbf{v}, \mathbf{v})_\Omega}. \quad (\text{A } 3)$$

The distance  $D$  between two velocity fields is based on this norm,

$$D(\mathbf{v}, \mathbf{w}) = \|\mathbf{v} - \mathbf{w}\|_\Omega. \quad (\text{A } 4)$$

The inner product (A 2) uniquely defines the snapshot POD (see, e.g., Holmes *et al.* 2012). The  $m$ th snapshot is represented by

$$\mathbf{u}^m(\mathbf{x}) := \mathbf{u}_0(\mathbf{x}) + \sum_{i=1}^{M-1} a_i^m \mathbf{u}_i(\mathbf{x}), \quad (\text{A } 5)$$

where  $\mathbf{u}_0$  denotes the mean flow,  $\mathbf{u}_i$  the  $i$ th POD mode and  $a_i^m$  the POD mode amplitude corresponding to the  $m$ th snapshot. It may be noted that the maximal number of POD modes is  $M - 1$ , e.g., two snapshots define a one-dimensional line, not a plane.

Let  $\mathbf{v} = \mathbf{u}_0 + \sum_{i=1}^{M-1} b_i \mathbf{u}_i$  and  $\mathbf{w} = \mathbf{u}_0 + \sum_{i=1}^{M-1} c_i \mathbf{u}_i$  be two velocity field representations, e.g., a snapshot and a centroid. Then, their distance is given by

$$D(\mathbf{v}, \mathbf{w})_\Omega = \sqrt{\sum_{i=1}^{M-1} (b_i - c_i)^2}. \quad (\text{A } 6)$$

Evidently, (A 6) is much quicker to compute than (A 4) assuming the typical case that the number of grid points is much larger than the number of snapshots.

## REFERENCES

- ASHURST, W. T. & MEIBURG, E. 1988 Three-dimensional shear layers via vortex dynamics. *J. Fluid Mech.* **189**, 87–116.
- BURKARDT, J., GUNZBURGER, M. & LEE, H. C. 2006 Centroidal Voronoi tessellation-based reduced-order modeling of complex systems. *SIAM J. Sci. Computing* **28** (2), 459–484.
- CAO, Y., KAISER, E., BOREÉ, J., NOACK, B. R., THOMAS, L. & GUILAN, S. 2014 Cluster-based analysis of cycle-to-cycle variations. Application to internal combustion engines. *Exp. Fluids* **55**, Article 1837:1–8.
- COATS, C.M. 1997 Coherent structures in combustion. *Prog. Energy Combust. Sci.* **22**, 427–509.
- COMTE, P., SILVESTRI, J. H. & BÉGOU, P. 1998 Streamwise vortices in Large-Eddy Simulations of mixing layer. *Eur. J. Mech. B* **17**, 615–637.
- DELVILLE, J., UKEILEY, L., CORDIER, L., BONNET, J. P. & GLAUSER, M. 1999 Examination of large-scale structures in a turbulent plane mixing layer. Part 1. Proper orthogonal decomposition. *J. Fluid Mech.* **391**, 91–122.
- FERNEX, D., SEMANN, R., ALBERS, M., MEYSONNAT, P. S., SCHRÖDER, W., ISHAR, R., KAISER, E. & NOACK, B. R. 2019 Cluster-based network model for drag reduction mechanisms of an actuated turbulent boundary layer. *Proc. Appl. Math. Mech.* **19** (1), 1–2.
- FIEDLER, H. & FERNHOLZ, H. H. 1990 On the management and control of turbulent shear flows. *Progr. Aeronaut. Sci.* **27**, 305–387.
- GOMEZ, F., BLACKBURN, H. M., RUDMAN, M., SHARMA, A. S. & MCKEON, B. J. 2016 A reduced-order model of three-dimensional unsteady flow in a cavity based on the resolvent operator. *J. Fluid Mech.* **798**, R2–1..14.
- HAMA, F. R. 1962 Streaklines in a perturbed shear flow. *Phys. Fluids* **5**, 644–650.
- HOLMES, P., LUMLEY, J. L., BERKOOZ, G. & ROWLEY, C. W. 2012 *Turbulence, Coherent Structures, Dynamical Systems and Symmetry*, 2nd edn. Cambridge: Cambridge University Press.
- ISHAR, R., KAISER, E., MORZYŃSKI, M., ALBERS, M., MEYSONNAT, P., SCHRÖDER, W. & NOACK, B. R. 2019 Metric for attractor overlap. *J. Fluid Mech.* **874**, 720–752.
- KAISER, E., NOACK, B. R., CORDIER, L., SPOHN, A., SEGOND, M., ABEL, M. W., DAVILLER, G., ÖSTH, J., KRAJNOVIĆ, S. & NIVEN, R. K. 2014 Cluster-based reduced-order modelling of a mixing layer. *J. Fluid Mech.* **754**, 365–414.
- KAISER, E., NOACK, B. R., SPOHN, A., CATTAFESTA, L. N. & MORZYŃSKI, M. 2017 Cluster-based control of nonlinear dynamics. *Theor. Comput. Fluid Dyn.* **31** (5–6), 1579–593.
- KASTEN, J., REININGHAUS, J., HOTZ, I., HEGE, H. C., NOACK, B. R., DAVILLER, G., COMTE, P. & MORZYŃSKI, M. 2016 Acceleration feature points of unsteady shear flows. *Arch. Mech.* **68**, 55–80.
- LIU, J. T. C. 1989 Coherent structures in transitional and turbulent free shear flows. *Ann. Rev. Fluid Mech.* **21**, 285–315.
- LLOYD, S. 1982 Least squares quantization in PCM. *IEEE Trans. Inform. Theory* **28** (2), 129–137.
- LORENZ, E. N. 1963 Deterministic nonperiodic flow. *J. Atm. Sci.* **20**, 130–141.
- MACQUEEN, J. 1967 Some methods for classification and analysis of multivariate observations. *Proc. of the Fifth Berkeley Symp. On Math. Stat. and Prob.* **1**, 281–297.
- MANTIĆ-LUGO, V., ARRATIA, C. & GALLAIRE, F. 2014 Self-consistent mean flow description of the nonlinear saturation of the vortex shedding in the cylinder wake. *Phys. Rev. Lett.* **113** (8), 084501.
- MARDIA, K. V., KENT, J. T. & BIBBY, J. M. 1979 *Multivariate Analysis*. Academic Press.
- MICHALKE, A. 1964 On the inviscid instability of the hyperbolic-tangent velocity profile. *J. Fluid Mech.* **19**, 543–556.
- MONKEWITZ, P. A. 1988 Subharmonic resonance, pairing and shredding in the mixing layer. *J. Fluid Mech.* **188**, 223–252.
- NAIR, A., YEH, C. A., KAISER, E., NOACK, B. R., BRUNTON, S. L. & TIARA, K. 2019 Cluster-based feedback control of turbulent post-stall separated flows. *J. Fluid Mech.* **875**, 345–375.
- NAIR, A. G. & TAIRA, K. 2015 Network-theoretic approach to sparsified discrete vortex dynamics. *J. Fluid Mech.* **768**, 549–571.



- NEWMAN, M. 2010 *Networks: An Introduction*. Oxford University Press.
- NOACK, B. R. 2016 From snapshots to modal expansions – bridging low residuals and pure frequencies. *J. Fluid Mech. – Focus in Fluids* **802**, 1–4.
- NOACK, B. R., PAPAS, P. & MONKEWITZ, P. A. 2005 The need for a pressure-term representation in empirical Galerkin models of incompressible shear flows. *J. Fluid Mech.* **523**, 339–365.
- NOACK, B. R., SCHLEGEL, M., AHLBORN, B., MUTSCHKE, G., MORZYŃSKI, M., COMTE, P. & TADMOR, G. 2008 A finite-time thermodynamics of unsteady fluid flows. *J. Non-Equilibrium Thermodyn.* **33**, 103–148.
- NOACK, B. R., STANKIEWICZ, W., MORZYŃSKI, M. & SCHMID, P. J. 2016 Recursive dynamic mode decomposition of transient and post-transient wake flows. *J. Fluid Mech.* **809**, 843–872.
- PASTOOR, M., KING, R., NOACK, B. R., KING, R. & TADMOR, G. 2005 Observers and feedback control for shear layer vortices. In *44th IEEE Conference on Decision and Control and European Control Conference ECC 2005*. Seville, Spanien, 12.–15. Dezember 2005.
- PROTAS, B., NOACK, B. R. & ÖSTH, J. 2015 Optimal nonlinear eddy viscosity in Galerkin models of turbulent flows. *J. Fluid Mech.* **766**, 337–367.
- ROWLEY, C. W., MEZIĆ, I., BAGHERI, S., SCHLATTER, P. & HENNINGSON, D. S. 2009 Spectral analysis of nonlinear flows. *J. Fluid Mech.* **645**, 115–127.
- SASAKI, K., TISSOT, G., CAVALIERI, A. V. G., SILVESTRE, F. J., JORDAN, P. & BIAU, D. 2018 Closed-loop control of a free shear flow: a framework using the parabolized stability equations. *Theor. Computat. Fluid Dyn.* **32** (6), 765–788.
- SCHLEGEL, M. & NOACK, B. R. 2015 On long-term boundedness of Galerkin models. *J. Fluid Mech.* **765**, 325–352.
- SCHMID, P. J. 2010 Dynamic mode decomposition for numerical and experimental data. *J. Fluid Mech.* **656**, 5–28.
- SHAQARIN, T., NOACK, B. R. & MORZYŃSKI, M. 2018 The need for prediction in feedback control of a mixing layer. *Fluid Dyn. Res.* **50**, 1–22.
- SPARROW, C. 1982 *The Lorenz Equations: Bifurcations, Chaos, and Strange Attractors*, 1st edn. *Applied Mathematical Sciences* 41. New York: Springer-Verlag.
- STEINHAUS, H. 1956 Sur la division des corps matériels en parties. *Bull. Acad. Polon. Sci.* **4** (12), 801–804.
- STUART, J. T. 1971 Nonlinear stability theory. *Ann. Rev. Fluid Mech.* **3**, 347–370.
- TAIRA, K., NAIR, A. G. & BRUNTON, S. L. 2016 Network structure of two-dimensional decaying isotropic turbulence. *J. Fluid Mech.* **795**.
- UKEILEY, L., CORDIER, L., MANCEAU, R., DELVILLE, J., BONNET, J. P. & GLAUSER, M. 2001 Examination of large-scale structures in a turbulent plane mixing layer. Part 2. Dynamical systems model. *J. Fluid Mech.* **441**, 61–108.
- WEI, M. & ROWLEY, C. W. 2009 Low-dimensional models of a temporally evolving free shear layer. *J. Fluid Mech.* **618**, 113–134.